Available online at www.sciencedirect.com

ScienceDirect

journal homepage: www.elsevier.com/locate/he

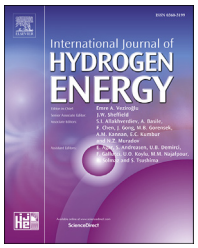

Advances in unit operations and materials for the Cu–Cl cycle of hydrogen production

G.F. Naterer [a,*], S. Suppiah [b], M.A. Rosen [c], K. Gabriel [c], I. Dincer [c], O.A. Jianu [c], Z. Wang [e], E.B. Easton [h], B.M. Ikeda [d], G. Rizvi [c], I. Pioro [d], K. Pope [a], J. Mostaghimi [f], S.N. Lvov [g]

[a] Memorial University of Newfoundland, St. John's, Newfoundland, A1B 3X5, Canada
[b] Hydrogen Isotopes Technology Branch, Canadian Nuclear Laboratories, Chalk River, Ontario, K0J 1J0, Canada
[c] Faculty of Engineering and Applied Science, University of Ontario Institute of Technology (UOIT), 2000 Simcoe Street North, Oshawa, Ontario, L1H 7K4, Canada
[d] Faculty of Energy Systems and Nuclear Science, University of Ontario Institute of Technology (UOIT), 2000 Simcoe Street North, Oshawa, Ontario, L1H 7K4, Canada
[e] College of Energy, Xiamen University, Xiamen City, Fujian Province, 361102, China
[f] Centre for Advanced Coatings Technologies, University of Toronto, Toronto, Ontario, M5S 3E5, Canada
[g] Pennsylvania State University, 207 Hosler Building, University Park, PA, 16802, USA
[h] Faculty of Science, University of Ontario Institute of Technology (UOIT), 2000 Simcoe Street North, Oshawa, Ontario, L1H 7K4, Canada

ARTICLE INFO

Article history:
Received 20 January 2017
Received in revised form
4 March 2017
Accepted 6 March 2017
Available online 2 June 2017

Keywords:
Thermochemical copper–chlorine cycle for hydrogen production
Electrochemical cell
Thermolysis
Hydrolysis
Materials corrosion
Materials coatings

ABSTRACT

This paper presents recent advances by an international team of five countries – Canada, U.S., China, Slovenia and Romania – on the development and scale-up of the copper–chlorine (Cu–Cl) cycle for thermochemical hydrogen production using nuclear or solar energy. Electrochemical cell analysis and membrane characterization for the CuCl/HCl electrolysis process are presented. Constituent solubility in the ternary CuCl/HCl/H_2O system and XRD measurements are reported in regards to the $CuCl_2$ crystallization process. Materials corrosion in high temperature copper chloride salts and performance of coatings of reactor surface alloys are examined. Finally, system integration is examined, with respect to scale-up of unit operations, cascaded heat pumps for heat upgrading, and linkage of heat exchangers with solar and nuclear plants.

* *Corresponding author*. Faculty of Engineering and Applied Science, Memorial University of Newfoundland, St. John's, Newfoundland, A1B 3X5, Canada.
E-mail address: gnaterer@mun.ca (G.F. Naterer).
http://dx.doi.org/10.1016/j.ijhydene.2017.03.133

Introduction

The copper–chlorine (Cu–Cl) cycle of thermochemical water splitting is a promising method for large-scale hydrogen production from nuclear, solar or other thermal energy sources [1,2]. It offers significant advantages over other thermochemical cycles such as lower temperature operating requirements (below 550 °C) and the ability to effectively utilize low-grade waste heat for endothermic processes. It consists of four main steps: 1) hydrolysis, 2) thermolysis, 3) electrolysis, and 4) water separation (e.g. crystallization) [3–5] – which together split water into hydrogen and oxygen through intermediate copper and chlorine compounds. Other thermochemical cycles have been identified in a Nuclear Hydrogen Initiative [6], and this includes the sulfur-iodine [7], cerium-chlorine [8] and iron-chlorine [9] cycles. Funk [10] and Naterer et al. [11] presented comprehensive reviews of hydrogen production by thermochemical water decomposition.

In the CuCl/HCl electrolysis step, oxidation of copper (I) chloride (CuCl) during an electrochemical reaction occurs in the presence of hydrochloric acid (HCl) to generate hydrogen. The Cu(I) ion is oxidized to Cu(II) at the anode, and the hydrogen ion is reduced at the cathode. This CuCl/HCl electrolysis process was first demonstrated for a long duration by Canadian Nuclear Laboratories (CNL) [12,13]. Continuous electrolysis for 1600 h was demonstrated in a cell operating at a voltage of about 0.7 V at 45 °C [3]. Significant developments in CuCl/HCl electrolysis have also been demonstrated experimentally at Pennsylvania State University [14] and the University of Ontario Institute of Technology [15]. Various membranes have been investigated to mitigate the adverse effects of copper crossover [16]. Nafion-based and porous polyethylene (PPE) membranes have been found to inhibit copper transport with HCl as a catholyte [17,18]. It was shown that the current efficiency is more than 95% when the cell potential is stable at 0.7 V, and the current density is 0.5 A cm^{-2} for a 36 h test using a Nafion-based membrane.

Early studies of the Cu–Cl cycle used a spray drying process to extract solid $CuCl_2$ from the aqueous solution exiting the electrochemical cell. However, this was subsequently determined to be energy intensive, and led to undesirable vaporization of other compounds; so alternatives such as crystallization were explored. Wang et al. [19] reported on the integration of electrolysis and hydrolysis steps using crystallization of $CuCl_2$ particles from the electrochemical cell. Leray [20] and Abdel [21] had previously examined the growth kinetics of hydrated copper (II) chloride ($CuCl_2 \cdot n_h H_2O$, where n_h is the number of hydrated water molecules) and the recovery of cupric chloride from spent solutions. Crystallization of $CuCl_2$ is normally less energy intensive than spray drying because ambient air and cooling water can be sufficient for cooling the solution to ambient temperature.

Copper (II) chloride is the oxidation product of copper (I) chloride, hence copper (II) and copper (I) chlorides coexist in the aqueous solution of HCl. The solubility of copper (I) chloride (CuCl) in aqueous hydrochloric acid (HCl) at different molarities and temperatures [22–25] affects the crystallization process. The solubility of solid CuCl in aqueous HCl is much larger than in water [25]. The crystal sizes of the chloro complexes and the conversion rates from CuCl to $CuCl_2$ have been reported by O'Connor et al. [26]. Experiments were performed by Fritz [27] to determine the solubility of copper (I) chloride in various aqueous chlorides and their associated equilibrium constants of formation. A set of viral parameters expressing the activity coefficients of the ions formed by dissolution were found. These past studies found that the solubility of CuCl is increased by the presence of a relatively low concentration of HCl compared to the solubility in water.

The hydrolysis reaction is an endothermic non-catalytic gas–solid reaction at temperatures between 350 °C and 400 °C where $CuCl_2$ particles from the crystallization process are reacted with superheated steam to produce copper oxychloride solid ($CuOCuCl_2$, often denoted as Cu_2OCl_2) and hydrogen chloride (HCl). Extensive experimental studies with a spray reactor heated by a mixture of argon/steam [28,29] were conducted at the Argonne National Laboratory (ANL) to determine the mass flow rate of steam required to produce Cu_2OCl_2. Results indicated that 100% yields of Cu_2OCl_2 could be achieved with an ultrasonic nozzle to inject the reactants into the reactor at about 375 °C. The excess steam required for the heat supply reduces the overall cycle efficiency of the system. Pope et al. [30] examined the use of nitrogen to reduce the steam requirement of the hydrolysis reaction in a fluidized bed reactor. Equilibrium conversion rates, thermophysical properties of compounds, and a gas film layer around the solid $CuCl_2$ particles are significant factors that influence the hydrolysis reaction [31,32].

Materials of construction are major issues in the Cu–Cl cycle development. Limited data exists in past literature on the corrosion resistance of materials in molten CuCl. The most suitable materials for high temperature and corrosive environments are ceramics, refractory metals, molybdenum and nickel based alloys, graphite based materials, and Hastelloy C. Xie et al. [33] examined the corrosion of carbide/nitride materials in 2.5 mol/L HCl solutions at elevated temperatures. Wu et al. [34] tested mullite specimens in a 10 wt.% NaOH solution at 105 °C and examined a sol–gel coating to improve corrosion resistance. They have identified that the process of forming mullite has a significant impact on its ability to resist corrosion. Sure et al. [35] reported the performance of partially stabilized zirconia (PSZ) with graphite coatings at 600 °C and found that PSZ corroded by adding oxygen to the surface. Experimental findings of the corrosion of graphite in molten LiCl, and graphite powder mixed with 46 wt.% LiCl that were melted to change the molten salt structure, were reported by Kamali and Fray [36]. The corrosion behavior of Hastelloy C276, C-22 and N were examined at 250 and 500 °C in dry molten salt with a composition of 13.4 mol% NaCl, 33.7 mol% KCl and 52.9 mol% $ZnCl_2$ (Vignarooban et al. [37]). Sellers et al. [38] investigated the corrosion rates of Hastelloy N and 316 stainless Steel immersed for 100 h at 850 °C in a molten salt consisting of 46.5 mol% LiF, 11.5 mol % NaF and 42 mol% KF. Siantar [39] conducted experiments to examine the performance of metallic and ceramic coatings on a base metal exposed to molten CuCl at 500 °C.

A number of other related studies associated with the Cu–Cl cycle were conducted by the international team including exergo-economics using exergy-cost-energy-mass (EXCEM) analysis [40,41], life cycle analysis [42], environmental impacts

[43], applications in the transportation sector [44], and integrated systems with geothermal energy [45], solar energy [46,47], and desalination plants [48]. The team is collaborating on the development of enabling technologies for the Cu–Cl cycle, through the Generation IV International Forum (GIF). This paper describes the progress of development of these enabling technologies, particularly focusing on recent advances presented at workshops in 2015 and 2016 in Oshawa, Ontario [49,50], involving CuCl/HCl electrolysis, crystallization, constituent solubility in ternary mixtures, materials corrosion, and scale-up of unit operations.

Thermochemical copper chlorine (Cu–Cl) cycle

The 4-step Cu–Cl cycle consists of a sequence of four main steps: 1) hydrolysis (water splitting), 2) thermolysis (oxygen production), 3) electrolysis (hydrogen production), and 4) water separation by crystallization or spray drying.

- Step 1: Hydrolysis (endothermic)

$$2CuCl_2 \cdot n_h\, H_2O\ (l) + H_2O\ (g) \leftrightarrow CuOCuCl_2\ (s) + 2HCl\ (g) + n_h H_2O\ (g) \quad (1)$$

where $n_h = 0–4$ at 400 °C, $\Delta H = 27.9$ kcal/mol.

- Step 2: Thermolysis (endothermic)

$$CuOCuCl_2\ (s) \leftrightarrow 2CuCl\ (l) + 0.5O_2\ (g) \quad (2)$$

at 530 °C, $\Delta H = 30.9$ kcal/mol.

- Step 3: Electrolysis

$$2CuCl\ (aq) + 2HCl\ (aq) \leftrightarrow 2CuCl_2\ (aq) + H_2\ (g) \quad (3)$$

in aqueous solution of HCl, at 90 °C, $\Delta H = 22.4$ kcal/mol.

- Step 4: Water separation (endothermic)

$$CuCl_2\ (aq) + n_f H_2O\ (l) \leftrightarrow CuCl_2 \cdot n_h H_2O\ (s) + (n_f - n_h)H_2O\ (g/l) \quad (4)$$

where n_f and n_g represent the amount of water molecules in liquid and gaseous states, respectively, and $n_f > 7.5$, $n_h = 0–4$ at 30–80 °C (crystallization) or 100–260 °C (spray drying).

This water splitting process begins when water enters the thermochemical plant, recovers heat, forms steam, enters the hydrolysis reactor, and then reacts with copper (II) chloride (solid) to form copper oxychloride (solid) and hydrogen chloride gas. The HCl/H_2O gas leaves the hydrolysis reactor, condenses in an aqueous solution, and enters the electrolysis reactor. The exiting copper oxychloride particles are transported to the thermolysis reactor and decomposed to produce oxygen gas and molten CuCl. Molten CuCl overflows out of the thermolysis reactor into a water bath thus generating steam and solidifying to form a water/CuCl slurry. The slurry is moved to the electrolyzer via a dissolution cell where CuCl dissolves in HCl (aq) to form a ternary $H_2O/HCl/CuCl$ aqueous solution. This aqueous solution is then pumped to the electrolyzer anode.

CuCl/HCl electrolysis

Electrochemical cell analysis

Analysis of the electrochemical kinetic equations has been performed to predict the equilibrium state limitations on the anode side of the electrolyzer [49]. Concentrations were determined for anolyte species and sensitivity analyses of equilibrium states were conducted at varying temperatures. With reference to Fig. 1, five overall reactions occur in the electrochemical cell.

- Dissociation : $CuCl(s) \Leftrightarrow Cu^+(aq) + Cl^-(aq)$ (5)
- Dissociation : $HCl(l) \Leftrightarrow H^+(aq) + Cl^-(aq)$ (6)
- Oxidation : $Cu^+(aq) \Leftrightarrow Cu^{+2}(aq) + e^-$ (7)
- Precipitation : $Cu^{+2}(aq) + 2Cl^- \Leftrightarrow CuCl_2(aq)$ (8)
- Reduction : $H^+(aq) + e^- \Leftrightarrow 0.5H_2(g)$ (9)

Reactions (5) and (6) occur in the $CuCl–HCl–H_2O$ region of the anolyte tank where CuCl and HCl dissociate into their ions, respectively. Depending on concentrations, CuCl(s) dissociation might be incomplete after passing the solubility limit. The solution pumped to the anode side of the cell has aqueous ions. Equations (7) and (8) represent oxidation of Cu(I) species on the anode surface and reduction of Cu^{2+} in the anolyte bulk solution. As reduction in Eq. (9) proceeds, hydrogen gas bubbles flow up toward the storage tank.

The anode half-cell was examined to find the equilibrium constant for Eq. (7) on the electrode and determine if the standard potential satisfies the equilibrium condition of Eq. (8). In the analysis, a copper ion loses an electron on the anode surface and free electrons out of the equilibrium barrier pass through the external circuit. Also, hydrogen ions are carried by water molecules as hydronium to the cathode side for hydrogen production. The equilibrium system is consistent for all three reactions, i.e., reactions (7) to (9).

An electrochemical model was developed for the electrolyzer cell and focused on the anode side to study the reaction kinetics [49]. Thermodynamic temperature-dependent properties for aqueous substances were used to relate the thermodynamics of the process to electrochemistry through the Gibbs free energy change of reactions. Furthermore, investigations were conducted to determine the variation of the standard potential for the anodic redox reaction with respect to temperature and ionic concentration changes.

Sample results from the analysis are shown in Fig. 2. As the temperature rises, the equilibrium concentration of Cu^{2+} decreases. It was found that a high anolyte temperature does not permit the anodic reaction to proceed to the products side, so electrons cannot readily flow through the external circuit in such conditions. Increasing the applied potential on the anode results in a redox reaction moving towards the product side. This effect is weaker at higher temperatures. Also, to establish

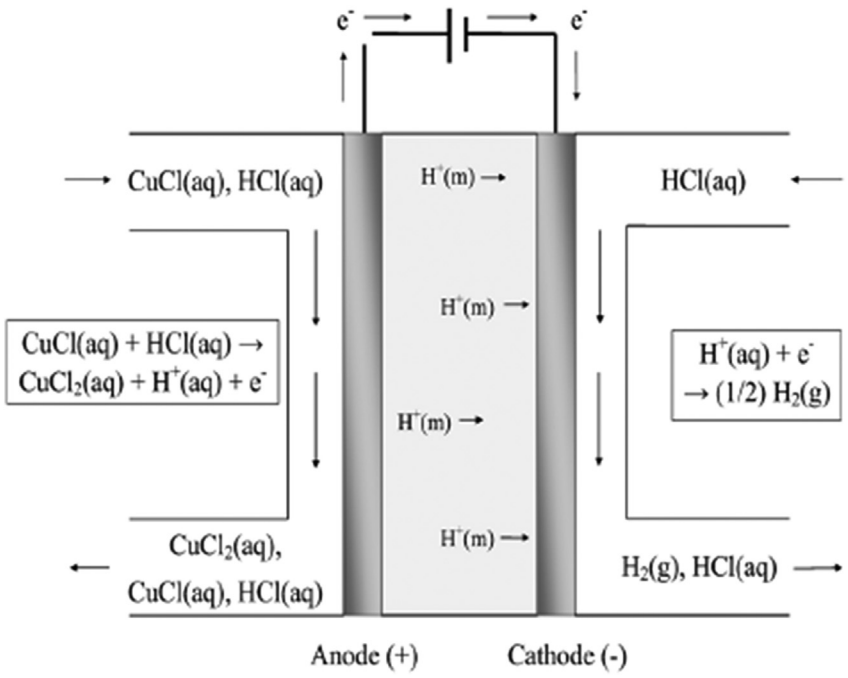

Fig. 1 – Schematic of the CuCl/HCl electrolyzer.

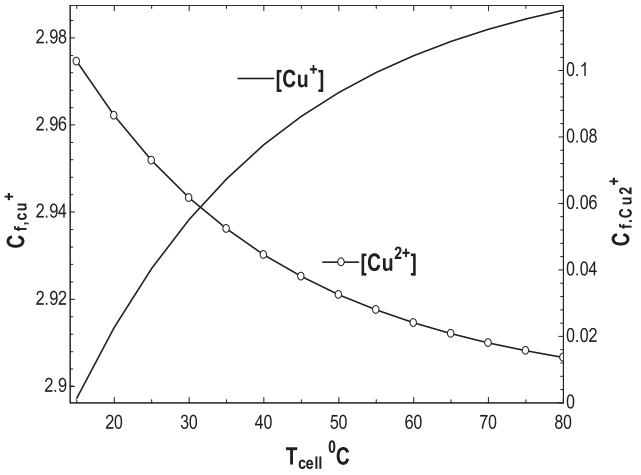

Fig. 2 – Effects of temperature on equilibrium concentrations of anodic reaction ions.

equilibrium for the anodic reaction and the $CuCl_2$ formation reaction under the same working conditions, the applied potential cannot be lower than 0.19 V (at 25 °C) since the standard redox potential at this temperature is 0.16 V.

Electrolysis membrane characterization

The core component of an electrochemical cell is a membrane electrode assembly (MEA) which generally uses a Nafion proton exchange membrane (PEM) since it is permeable to cations and neutral to species, hence allowing Cu to permeate the membrane and deposit on Pt catalytic sites via the cathode. Since this process drastically reduces the efficiency of the cell, several membranes, including Nafion/polypyrrole and Nafion/polyaniline composite membranes, have been examined [49] in the efforts to improve the performance. Hence the research team investigated the rate of Cu crossover and conductivity of the membranes in permeation and impedance spectroscopy tests.

The ion-exchange capacity (IEC), a measure of the H^+ ions that interact with the sulphonic groups, was determined through titration in order to determine the relative quantity of polyaniline (PANI) in the composite membranes. It was noticed that the IEC in the modified membranes decreased to 0.5 meq/g, as presented in Table 1. This drop in the IEC is a reflection of the amount of PANI interacting with the sulfonic groups in the composite membranes. This was expected as the PANI chains replaced the H^+ and interacted with the sulfonic groups thus decreasing the IEC due to a lower amount of

Table 1 – Physical properties of pristine Nafion and Nafion/PANI composite membranes [50].

Membrane	% water uptake	IEC (meq/g)	Conductivity S/cm	Permeability cm^2/s	Selectivity S/cm^3
N115	26.8	0.854	9.78E–02	6.86E–07	1.43E+05
N115-0.2M PANI	13.7	0.579	2.35E–02	4.20E–07	5.60E+04
N115-0.5M PANI	17.1	0.543	2.37E–02	3.76E–07	6.29E+04
N117	31.4	0.847	1.19E–01	1.05E–06	1.13E+05
N117-0.2M PANI	20.4	0.573	3.53E–02	4.94E–07	7.14E+04
N115-0.5M PANI	20.1	0.560	2.77E–02	4.78E–07	5.80E+04

protons available for exchange. This IEC decrease is observed in both PANI composite membranes (i.e. N115 and N117). Furthermore, increasing the aniline concentration from 0.2 M to 0.5 M had very little effect on the value of IEC.

Fig. 4 illustrates fuel cell H_2 cyclic voltammograms (CV) produced at a sweep rate of 50 mV s^{-1} at 25 °C. To detect Cu crossover during regular cell operation, the 2.0 M HCl was introduced on the left side of the electrochemical cell at 60 mL/min and the H_2 on the right side at 25 mL/min. The first day of the CV measurement, for all membranes, did not show any traces of copper deposition. Previously prepared Ppy composite membranes were used for comparison.

The CV measurement of N115/Ppy c membranes for the 3 days did not display any oxidation or reduction peaks at 0.4–0.5 V as can be seen in Fig. 3 (a), which could be a positive sign of the absence of any copper crossover. Fig. 3 (b) illustrates the CV measurements of the N115 pristine membrane. It clearly shows the oxidation and reduction peaks on the second and third testing days, whereas these peaks were absent on the first day. These peaks are attributed to the oxidation and reduction of copper accumulated as a result of crossover. The CV measurements obtained for N117/Ppy c and N117-0.2M PANI $FeCl_3$ 24 h c are shown in Fig. 3 (c) and (d), respectively. The CV measurements of N117/Ppy c membrane did not show any oxidation or reduction peaks for the first and second day. An oxidation peak appeared at 0.3 V without any clear reduction peak. This peak is not likely to represent the copper crossover as its potential does not match the value of 0.4–0.5 V. The CV measurements of N117-0.2M PANI $FeCl_3$ 24 h c membrane showed small oxidation reduction peaks as illustrated in Fig. 3 (d). These small peaks indicate that there was some copper deposition. The experiments found that N115/Ppy c performance was the best amongst the tested membranes.

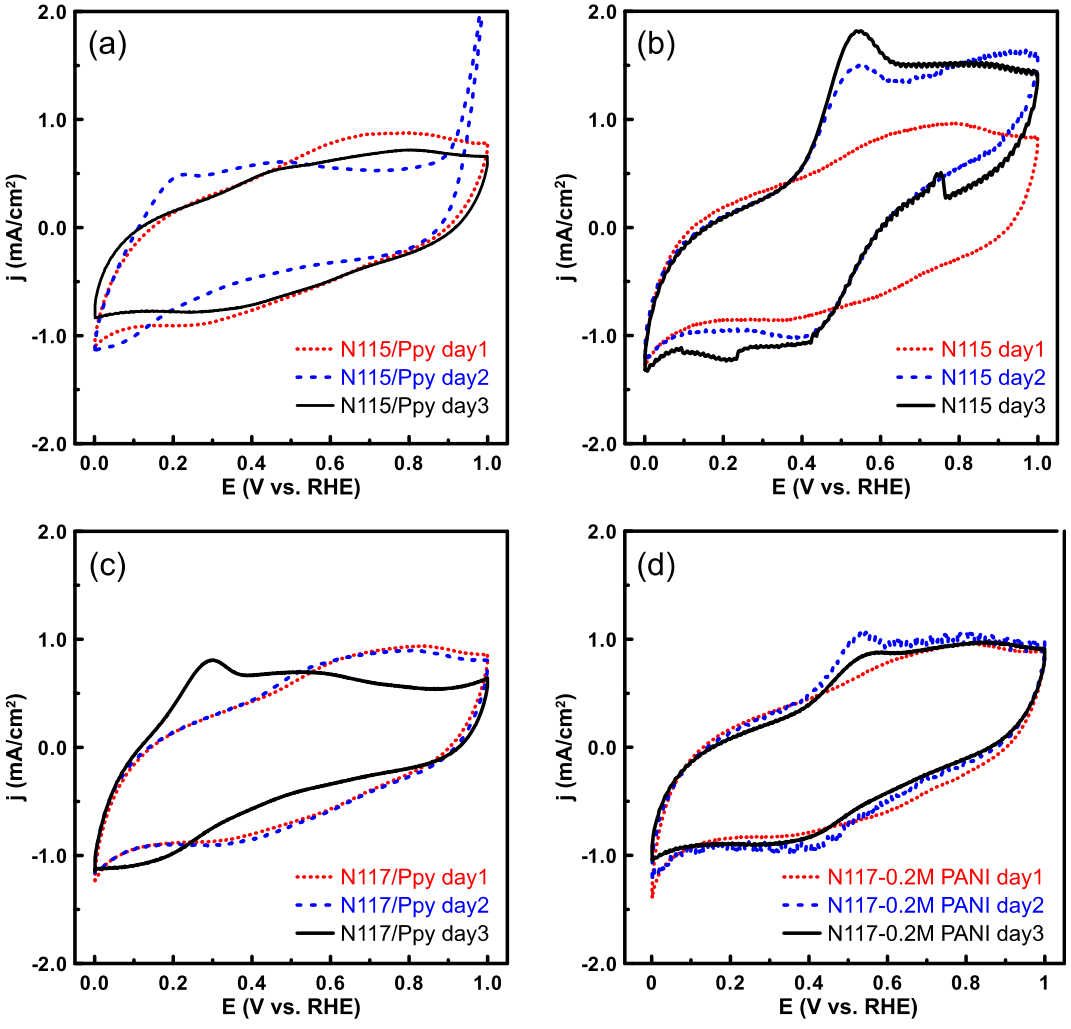

Fig. 3 – Diagnostic mode full cell CV for pure Nafion N115 membrane and other composite membranes after certain working days (abbreviated d). (a) N115/Ppy c (b) N115 (c) N117/Ppy (d) N117-0.2M PANI. Measurements were taken at a sweep rate of 50 mV s^{-1} at 25.0 °C with 2.0 M HCl flowing in the left side of the cell at 60 mL min^{-1} and H_2 flowing in the right side at 25 mL min^{-1}.

$CuCl_2$ crystallization

XRD measurements of $CuCl_2$ crystallization

Different methods have been considered to recover solids from the aqueous solution. Crystallization is a preferred option due to lower energy requirements. Experiments have been performed to determine the range of concentrations at which crystals of $CuCl_2$ can be extracted from the aqueous solution exiting the electrochemical cell.

It has been determined that a paste-like substance is obtained when the concentration exceeds 9 mol/L HCl and no crystallization occurs for concentrations below 3 mol/L HCl. The composition of the recovered solids was analyzed using X-ray diffraction (XRD). Thermochemical properties such as thermal stability and decomposition temperature were determined using thermogravimetric analysis (TGA), with one of the transition points on the TGA curve being identified to be around 442 °C. The crystals identified through XRD were $CuCl_2$ dihydrate (i.e., $CuCl_2 \cdot 2H_2O$) and botallackite. It was observed that crystallization propagates from an initial crystal and it is influenced by the crystallizing agent present in the solution (i.e. different molarity HCl). Additionally, for solutions with molarities below 5 mol/L, the crystallization occurs at a temperature below 30 °C.

Metastability of $CuCl_2$ in H_2O–HCl

The solid–liquid phase change process is dependent on the direction of temperature change (i.e., heating or cooling). During a heating process, the dissolving temperature increases whereas during cooling, the precipitation temperature decreases. The difference between these two temperatures is the Metastable Zone Width (MSZW). Precipitation occurs at a lower temperature thereby reducing the energy requirements of the phase change process. This process is a form of hysteresis. Dissolution occurs at a temperature of T_d and precipitation occurs at T_{met}, therefore, MSZW = $T_d - T_{met}$. Recent studies [52] investigated the MSZW for ternary solutions of water (H_2O), hydrogen chloride (HCl), and copper (II) chloride ($CuCl_2$). The study examined the effects of cooling rate and HCl concentration on MSZW, as well as the effect of HCl concentration and initial temperature on K_{sp} (solubility product constant).

In the experiments, a heated solution of known molarity was prepared with a concentration below saturation. The unsaturated solution was cooled at a controlled rate until a crystal appeared. The temperatures were recorded and the solution was then heated until the crystal re-dissolves. Again the temperature was recorded and the difference in temperatures is the MSZW.

The value of K_{sp} was calculated in terms of Gibbs free energy. A plot of ln(MSZW) and ln(cooling rate) was found to be nearly linear. Most data points were within ±1σ of the weighted average (Wt. Avg.) All points lie within ±2σ of the Wt. Avg. The cooling rate was correlated with the MSZW and nucleation rate constant, K_N,

$$\ln(\text{Cooling Rate}) = m \times \ln(\text{MSZW}) + \ln(K_N) \quad (10)$$

where m is the nucleation order (slope) that characterizes the nucleation process of crystal formation and K_N represents the nucleation rate constant ($\ln(K_N)$ corresponds to the y-intercept). Table 2 summarizes the resulting correlations at varying HCl concentrations.

As illustrated in Fig. 4, MSZW decreases with HCl concentration and increases with cooling rate, whereas Fig. 5 demonstrates that K_{sp} increases with temperature and decreases with HCl concentration. These trends are important for reducing the energy requirements associated with the crystallization process as more precise data on the precipitation temperature can lower the energy input. A larger MSZW is preferred since it lowers the crystallization (precipitation) temperature, thus reducing energy input requirements to the Cu–Cl cycle.

Materials corrosion

Material corrosion in molten copper chloride

An experimental apparatus was designed and built at UOIT to examine the corrosion resistance of various metal alloys to high temperature copper chloride salts. CuCl powder was placed in an alumina crucible and melted in a heating mantle with a maximum temperature of 600 °C. The alumina crucible

Table 2 – Nucleation order and nucleation rate constants for several HCl concentrations and temperature ranges between 25 °C and 65 °C.

HCl Concentration [M]	m	y-int	k_N	Number of data points
6	0.621	−6.16	2.11×10^{-3}	4
8	0.998	−6.06	2.34×10^{-3}	4
10	0.362	−5.59	3.73×10^{-3}	5
Mean	0.660	−5.94	2.64×10^{-3}	2.73×10^{-3}
Wt. avg	0.618	−5.89	2.77×10^{-3}	2.87×10^{-3}

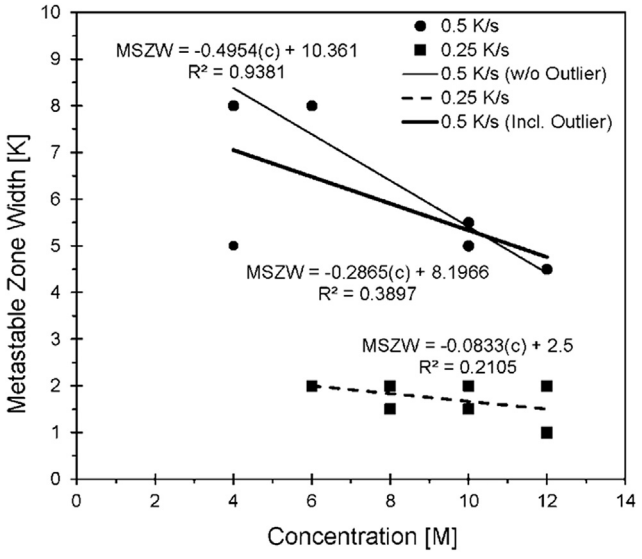

Fig. 4 – Effect of cooling rate on MSZW.

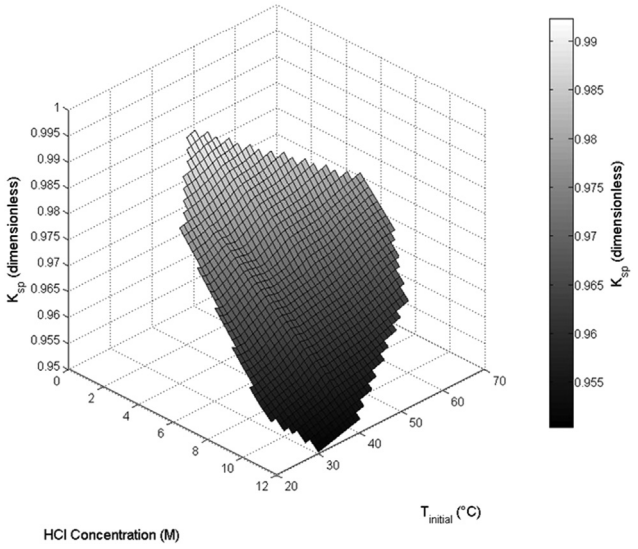

Fig. 5 – Solubility of $CuCl_2$ dissolving in HCl solutions of different molarities.

was used to avoid reactions between the crucible and molten salt. To ensure safety, the height of the crucible and inside diameter of the heating mantle were chosen so that tipping of the crucible inside the mantle and spilling of the molten salt are prevented. To ensure the environment is free of oxygen, the system is purged with high purity nitrogen prior and during experimentation. Several type K thermocouples are installed to measure the temperature of the molten salt and atmosphere outside the crucible. To prevent damage to the thermocouples in the molten salt, a thermal well consisting of a copper pipe is used. The copper does not react with the molten salt since the environment is free of oxygen. A standard 3-electrode arrangement is used to determine the corrosion behaviour.

Corrosion reactions involve the transfer of electrons and ions between the material and the solution. The rate of electron transfer is an electric current that depends on the potential difference between the metal and solution. The potential of the working electrode (corrosion sample) in the test solution under study was measured against a reference electrode with a voltmeter. A fixed potential is applied from a potentiostat connected to the working electrode and a counter electrode. The change in current at the working electrode caused by the applied potential forcing the oxidation reaction is then measured.

A review of past studies suggested that nickel chromium alloys would be the best candidates for the corrosive molten CuCl environment. These alloys have performed well in high temperature and highly corrosive environments, as well as chloride rich environments. The alloys tested in the corrosion experiments were: Inconel 625, Inconel 825, Inconel 686, Inconel Alloy 22, Hastelloy N, and Stainless Steel 316.

Samples were exposed to molten CuCl at 450 °C for various time intervals (2 h, 4 h, 8 h, 16 h, and 32 h) to determine the corrosion rate. All of the samples showed an impact of corrosion. All samples gained weight as a result of oxide phase formations, e.g., Cr_2O_3, Fe_2O_3, NiO. Also, all samples changed color as a result of the formation of an oxide layer. Many different colors were observed on the material surface, which is indicative of different thicknesses of oxide layers. The extent and rate of corrosion were determined by transient changes in weight. A weight gain on the samples was indicative of a layer of adherent corrosion product. Also, X-ray diffraction was used to determine the presence of crystalline oxide phases. The surface structure was identified by scanning electron microscope (SEM) imaging.

Fig. 6 illustrates the results of mass change per unit area for several alloys over time. Hastelloy was developed at Oak Ridge Laboratories for use in a liquid fluoride thorium reactor. It is a nickel alloy with high molybdenum content to prevent corrosion at high temperatures. Inconel 22 is a nickel and high chromium alloy (22 wt%) used primarily in chloride and fluoride environments. It exhibits corrosion resistance in cupric salt environments. Inconel 625 is typically used in high chloride environments, as well as high temperature air environments due to its high molybdenum and chromium content. Finally, Inconel 825 is a nickel-chrome alloy with an addition of titanium. Other alloys tested in the experiments include: Inconel 686 (nickel – chromium alloy) and Stainless 316 Iron alloy with an addition of chromium and molybdenum to aid in corrosion resistance.

A yellow crystallized solid formed at the top of the reactor. XRD results indicated that the crystal was copper (II) chloride dihydrate. As the top of the reactor is located outside of the furnace, a low temperature may have likely caused $CuCl_2$ to condense. No preferential deposition near the samples was observed, suggesting that the environment was constant around the experimental region. The corrosion rates are low as shown by the very small weight changes recorded over the test periods. The samples were exposed to the experiment conditions for long periods of time. Samples were analyzed by XRD and SEM imaging to determine the type of corrosion product found and surface characteristics.

Corrosion resistant coatings

Types of coatings

Molten salts used in industries are usually reactive with metallic surfaces as they are composed of a mixture of carbonates, nitrates or alkaline metals or halides of the alkaline-earth which usually form oxides that do not form a protective coating. As a consequence, an exchange of electrons occurs between the metal and the molten salts hence corrosion forms. Recent studies [49] reported the corrosion resistance of several metal alloys with various coatings in molten CuCl at 500 °C. Since medium carbon steel is known to form an oxidation layer hence slow down the corrosion mechanism, it was chosen as the base metal for the coatings experiments. Multiple specimens were investigated for corrosion starting with bare metal for oxidation tests. The different coatings described in Table 3 include metallic coating (i.e. Diamalloy 4006) and ceramic coating (i.e. Yttria-stabilized zirconia, YSZ).

Diamalloy 4006 is a Ni based amorphous alloy that exhibits an amorphous phase and microstructural homogeneity due to the absence of grain structures and microstructural features such as grain boundaries, micro segregation, and dislocations. The Zirconia based coatings were chosen for their superior

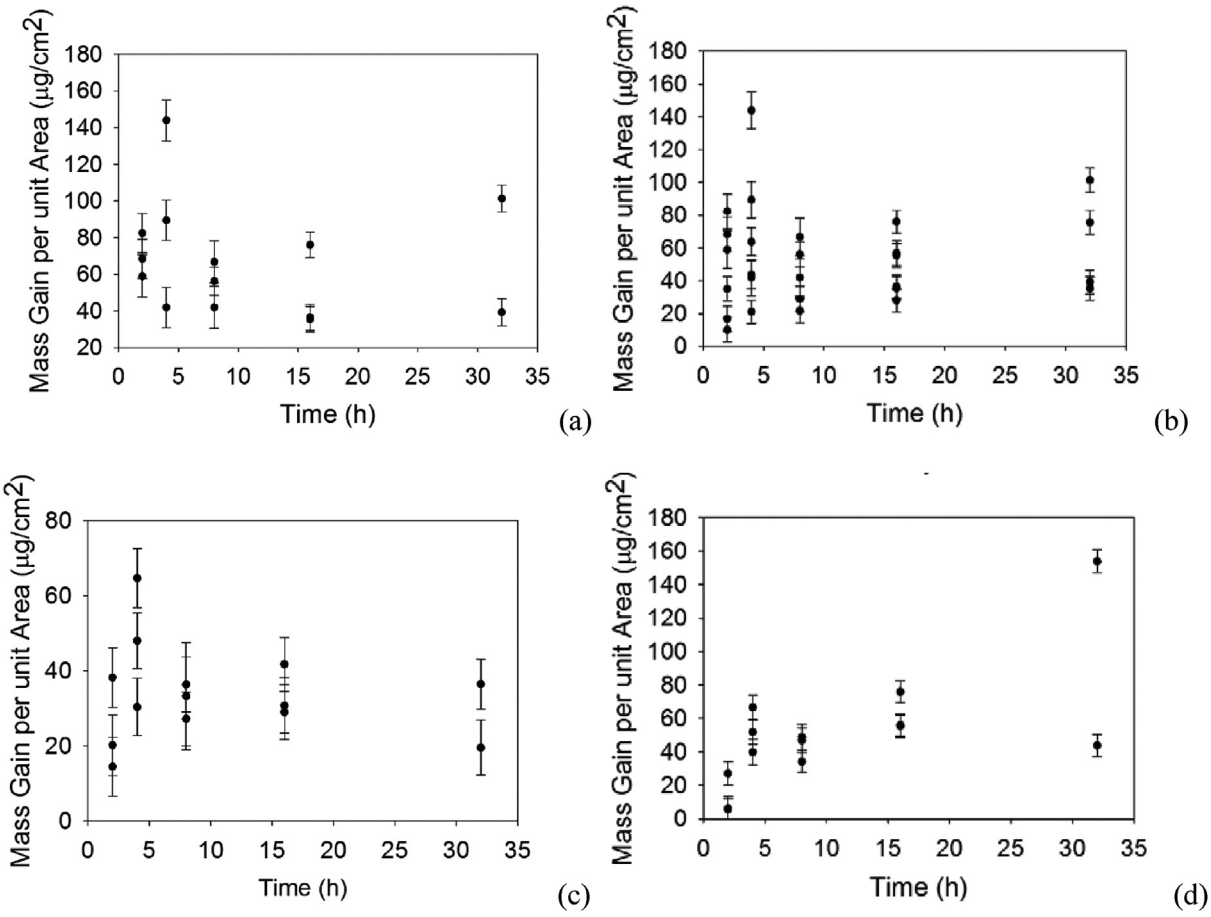

Fig. 6 – Mass gain per unit area for (a) Hastelloy N, (b) Inconel 22, (c) Inconel 625, and (d) Inconel 825.

Table 3 – List of sample coatings.

Coating	Sample	Abbreviation
0	Bare (uncoated) medium carbon steel – 1045	Mild
1	Medium carbon steel (1045) coated with YSZ coating	YSZ
2	Medium carbon steel (1045) coated with Diamalloy 4006 and YSZ coatings	Dia + YSZ
3	Medium carbon steel coated with Diamalloy 4006 and High velocity oxy-fuel coating spraying (HVOF)	Dia + HVOF

properties at high temperatures and resistance to corrosion in the presence of chlorine. Results based on similar coatings have been presented in Refs. [53] and [54].

Experimental apparatus

The immersion apparatus consists of an immersion test vessel (ITV), condenser vessel, scrubber vessel, and heating and control systems The fused quartz ITV lid is equipped with ports for thermocouples to record the temperature, gas exhaust and gas input. The exhaust gasses are scrubbed prior to being released via a condenser and scrubber. To prevent oxidation, the system is operated in the presence of nitrogen input via the gas input port. The lid is also equipped with a pressure relief valve and specimen handling device.

Exhaust gasses exiting the ITV are condensed in order to neutralize them before entering the scrubber and being released to the atmosphere via a fume hood. A 4.5 mol/L bicarbonate aqueous solution was used to scrub corrosive products from the exhaust fumes. A high temperature heating mantle was used to melt the CuCl whereas a PID controller kept the ITV contents at the desired temperature.

Each sample was examined visually before and after immersing it in the molten CuCl in order to identify a colour change that may characterize the corrosive products. A change in shape and pitting were observed in some specimens due to severe corrosion of the coating and/or base metal. The measurements were performed using optical devices. The change in weight of the samples before and after immersion was also recorded in order to determine the average corrosion penetration rate. To ensure that the corrosion is not due to oxygen trapped inside the system, an uncoated metal was immersed in the ITV and allowed to react with the oxygen present until the sample would exhibit no weight increase indicating an oxidation–reduction reaction.

Corrosion experimental results

(i) Coating 1 (YSZ Zirconia, ZrO_2 8%Y_2O_3)

A sample coated with coating #1 was immersed in the molten CuCl and allowed to react for 5 h. A green product indicating copper deposits was observed on the test specimen after extracting it from the ITV and cleaning it with saturated EDTA. EDX images confirmed the presence of copper on the sample surface (Fig. 7 a). Moreover, images revealed that the base metal was covered with a thin layer of YSZ and Cu. This indicates that Cu penetrated through the YSZ coating and attached to the surface of the base metal. It is anticipated that the YSZ coating did not have the required thickness to withstand the harsh test conditions and more tests with different YSZ thicknesses are necessary.

(ii) Coating 2 (Diamalloy 4006 + YSZ)

To determine the corrosion resistance capabilities of YSZ, a second test was performed for 48 h. This time the base metal sample was coated with a layer of metal-based coating (Diamalloy 4006) followed by a layer of ceramic-based coating (YSZ). This coating combination proved to have improved corrosion resistant properties in the molten CuCl (Fig. 7 b). Upon visual examination it was determined that the YSZ layer exhibited some delamination. It is likely that the delamination occurred due to differences in the thermal expansion of the different coating materials or CuCl attack in the molten state. Although some delamination was observed, the coating did not exhibit cracks hence no corrosion was observed on the base metal upon investigation with SEM and EXD.

(iii) Coating 3 (Diamalloy 4006 – HVOF)

High velocity oxy-fuel coating spraying (HVOF) is a thermal spray coating technique in which melted material is sprayed onto a substrate at high temperature with a specified velocity. Using this technique with Diamalloy 4006 produced the most promising results as the coating survived exposure to molten CuCl.

Figs. 8 and 9 illustrate the sample, before and after immersion tests, SEM and EDX images of the sample, respectively. Additional coatings were tested. Diamalloy 4006 with an Al_2O_3 top survived for 40 h. An SHS coating combination failed to survive for 100 h. Molten CuCl was splitting in some

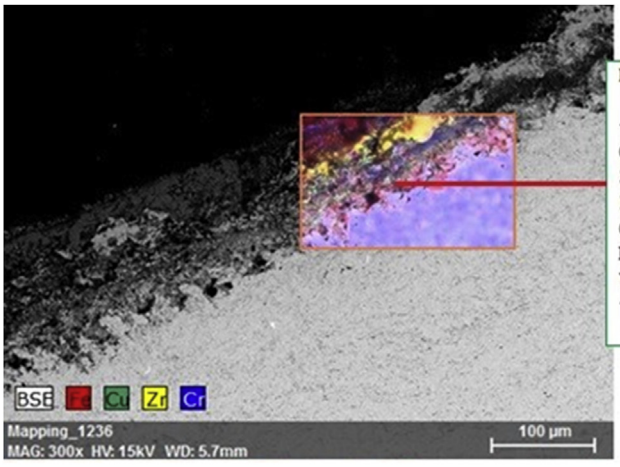

Element	AN	Series	Net unn. C [wt.%]	norm. C [wt.%]	Atom. C [at.%]
Copper	29	K-series	1072	20.07	45.65	46.04
Zirconium	40	L-series	1176	7.49	17.03	11.96
Iron	26	K-series	554	6.12	13.93	15.99
Chromium	24	K-series	517	4.96	11.28	13.90
Nickel	28	K-series	274	4.02	9.14	9.98
Yttrium	39	L-series	193	1.30	2.96	2.13
		Total:		43.96	100.00	100.00

(a)

Spectrum: Point

Element	AN	Series	Net unn. C [wt.%]	norm. C [wt.%]	Atom. C [at.%]
Iron	26	K-series	22335	88.29	89.90	71.09
Carbon	6	K-series	745	7.10	7.23	26.57
Manganese	25	K-series	562	1.64	1.67	1.34
Copper	29	K-series	107	0.91	0.93	0.65
Chlorine	17	K-series	230	0.28	0.28	0.35
		Total:	98.21	100.00	100.00	

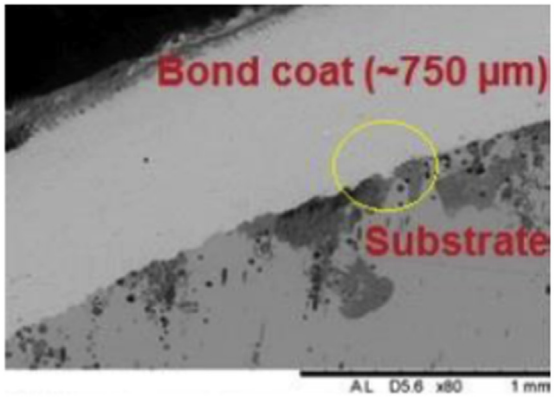

(b)

Fig. 7 – SEM/EDX images of sample #1 (a) (magnification: ×300; scale: 100 µm) and sample #2 (b) (Magnification: ×80, Scale: 1 mm).

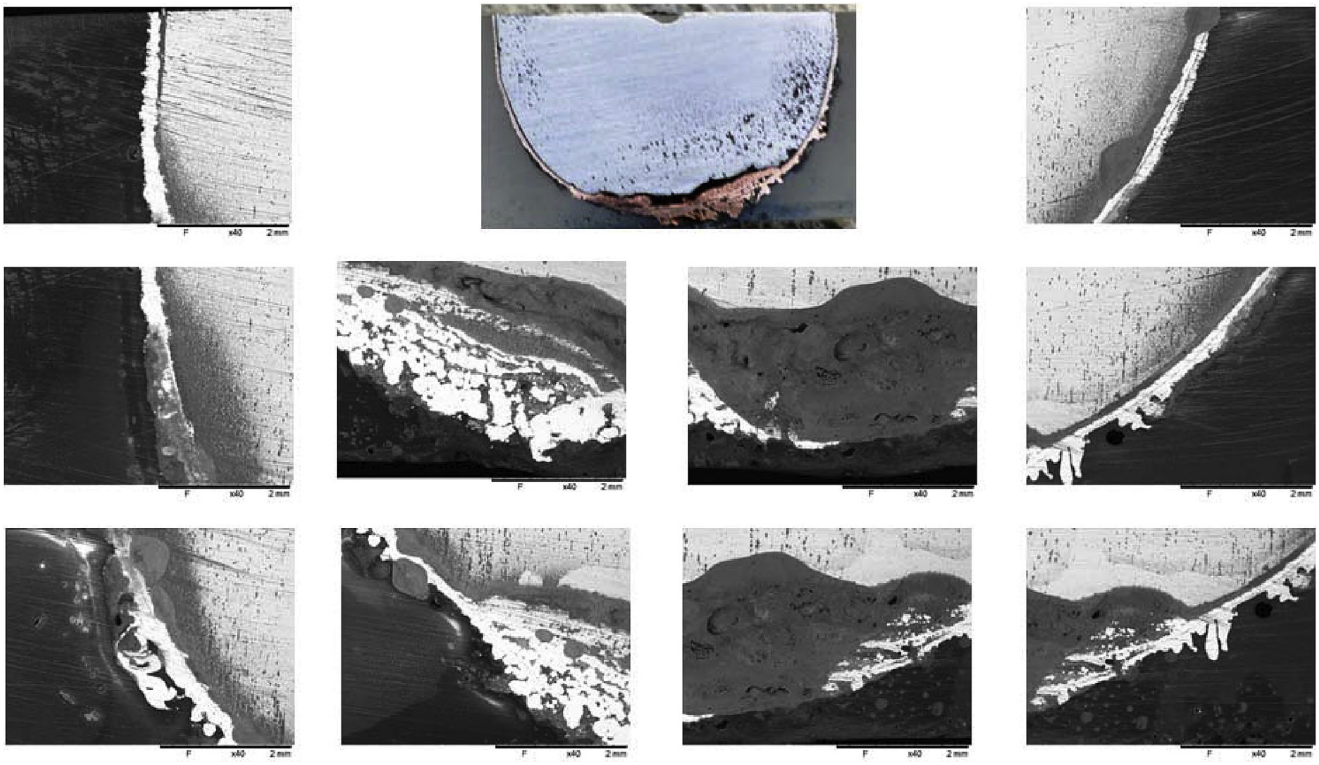

Fig. 8 – Scanning electron microscopy (SEM) images of sample #3 (Magnification: ×40, Scale: 2 mm).

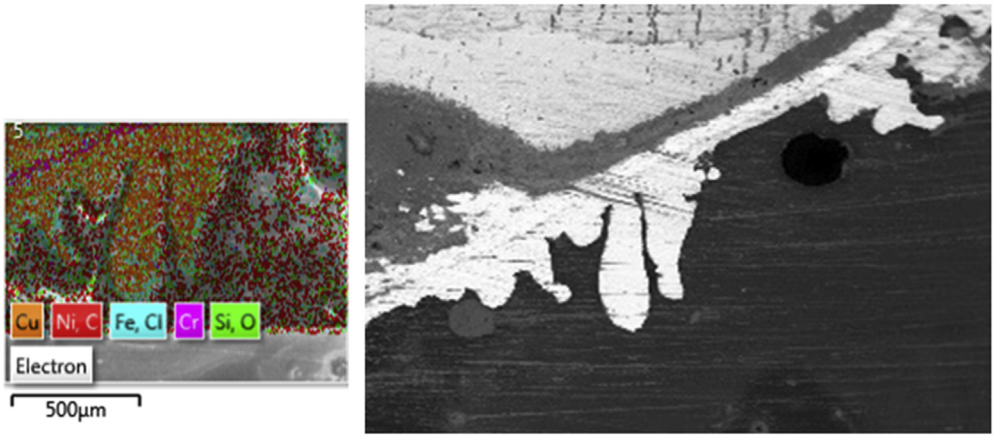

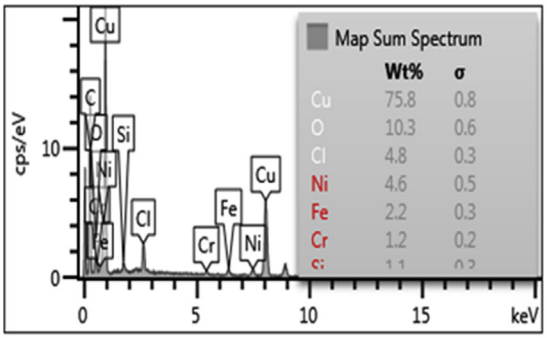

Ni	Cr	W	Mo	Cu	Fe	C	B
54	20.5	10	9	4	1	0.75	0.75

Fig. 9 – Energy dissipative X-ray spectroscopy (EDX) images of sample #3.

cases to form copper deposits on the sample. It was also found that Diamalloy coatings performed much better than SHS-9172. Overall, Diamalloy 4006 (HVOF) proved best in the group of tests conducted although the sample tip was damaged. Alloys under consideration for future testing include: Hastelloy, Quartz Glass coating (if possible), Udimet 500, IN718, nickel-based superalloy Nimonic105; and any potential corrosion resistant alloy.

System integration

Integration of lab-scale unit operations

A team of researchers at UOIT has reported numerous advances in the integration of experimental lab-scale unit operations of the Cu–Cl cycle in the Clean Energy Research Laboratory (CERL) [51]. This includes integration of the electrolysis/hydrolysis, thermolysis/hydrolysis, and transport systems between the unit operations. A low-temperature test loop was developed to integrate the electrolysis (anolyte loop), crystallization and dissolution cells. A new dilution and precipitation cell has been integrated to lower the HCl concentration in the flow stream. Also, a method to recover CuCl leaving the crystallization cell has been demonstrated.

For linkage of the electrolysis and hydrolysis steps, aqueous $CuCl_2$ is to be flash boiled into steam as it enters the hydrolysis reactor. The solution is pressurized to 2 MPa and heated to 200 °C. Heating is accomplished via heating tape wrapped around the inlet pipe to the hydrolysis reactor. The pre-boiling is performed to accelerate the hydrolysis reaction by increasing the thermal energy of reactants. Due to the constant flow required by integration of the processes, a new hydrolysis reactor has been designed. The new reactor design involves short pulses of fluid injection, allowing particles to settle out between pulses. Previous designs involving a cyclone separator were infeasible due to pulsating flow so an airlock system was selected instead. A rotary airlock at the bottom of the reactor allows for removal of $CuOCuCl_2$ salt. A heated "Clamshell" furnace allows for heating of steam within the reactor, in addition to heating the walls. The heated steam environment maximizes the rate of heat transfer. Then the solid powder of $CuOCuCl_2$ salt is extracted at a temperature of 400 °C and passed to the thermolysis reactor via screw conveyors. A schematic of the experimental layout is illustrated in Fig. 10.

For linkage of the hydrolysis and thermolysis reactors, as solid particles leave the hydrolysis reactor, a cooling step is necessary before the solid particles can be transported. Materials that can withstand exposure to $CuOCuCl_2$ and

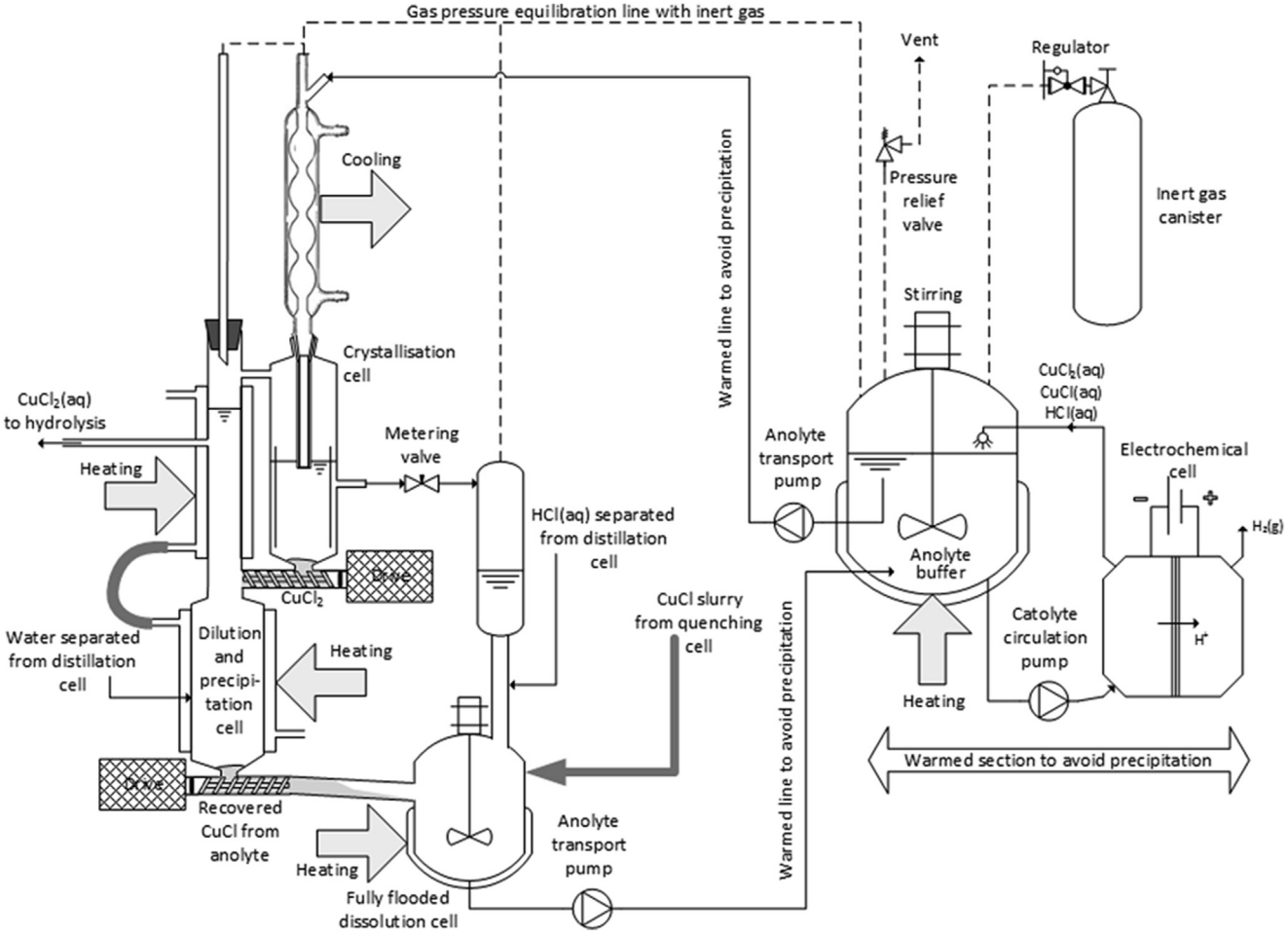

Fig. 10 – Layout of the integrated unit operations of the Cu–Cl cycle at UOIT.

other corrosive species are not heat resistant so the particles must be cooled. This is a challenging step to efficiently exchange heat from solids to a liquid. A flexible screw conveyor was used to convey the $CuOCuCl_2$ from the hydrolysis step to the oxygen reactor. The selection for the screw conveyor was based on 3 factors: temperature resistance, corrosion resistance, and flow rate. The screw conveyor is operated on a duty cycle to allow the heat exchanger time to cool down the particles.

The thermolysis reactor consists of an overflow vessel which melts the input of $CuOCuCl_2$ and overflows the output of liquid CuCl while venting oxygen gas to a fume hood. A current challenge with this reactor is to find a way to purge the system with an inert gas to prevent oxidation of the CuCl that is produced, as well as to purge the quench tube. A hydraulic tilt mechanism has been developed to allow a safe shutdown procedure of the oxygen reactor and purge liquid CuCl from the system. The tilt control will also allow for the control of flow rates into the quench, working in tandem with the conveyor to allow more accurate flow control.

The integration phase between the oxygen reactor and dissolution cells leads to the CuCl/HCl electrolyser. The slurry pump for CuCl transport must handle high temperature and highly corrosive solids.

Three options are available for cooled CuCl to be transported to the dissolution cells (as dry solids or wet slurry). Two designs involve dry solids, whereas another delivers a required flowrate of water-CuCl slurry.

In the first option, water-CuCl is removed from the quench tank and the slurry is pumped to the dissolution cell. A vibrating sieve collects the slurry and delivers CuCl solids to the dissolution cell. Then a pump recycles the separated water into the quench cell. The stoichiometric input for this integration phase to yield 0.1 kg of hydrogen per day requires a transported rate of CuCl from the oxygen reactor of approximately 0.41 kg/h. To optimize the amount of thermal energy transferred into the quench, the overflowed CuCl is dropped down a tube for heat recovery. The heat recovery allows for a much smaller quench bath vessel and an easier integration step. However, a significant difficulty is the possibility of oxidizing the falling CuCl. The process is completely purged with an inert gas.

In the second option, water-CuCl coming from the quench tank flows to a sifter. Water is then pumped back to the quench tank. The CuCl solids are placed on a conveyer and transported to the dissolution cell.

Thirdly, the water-CuCl slurry can instead be taken from the quench tank, at a desired concentration, by measuring the mass of collected CuCl. Then the slurry is pumped to the dissolution cell. This option assumes that water is pumped back to the quench tank from the hydrolysis reactor. In terms of energy utilization, this option is the most efficient approach. Of the three approaches considered, the slurry pump is the core component of system integration since it establishes transport at the desired concentration of water-CuCl that is required at the dissolution cell. Accurate knowledge of the ratios of CuCl to $CuCl_2$ is critical to allow for an efficient system to extract the $CuCl_2$, which is then fed to the hydrolysis reactor.

Intermediate heat exchanger for SCWR

The Canadian SuperCritical Water-cooled Reactor (SCWR) is a Generation IV concept of a future nuclear plant designed to operate at pressures of 25 MPa with reactor outlet temperatures up to 625 °C. These operating conditions make it a suitable candidate for hydrogen cogeneration with the thermochemical Cu–Cl cycle. Recent studies [49] have conducted an analysis of an intermediate heat exchanger linking a SCWR and Cu–Cl cycle. The Canadian SCWR concept consists of 336 fuel channels, with each channel housing a 5 m long fuel assembly. The core uses a pressurized inlet plenum that is connected to a low-pressure calandria vessel. The calandria vessel contains a heavy water moderator that will surround the 336 fuel channels. Each of the fuel channels contains a fuel assembly that features a central flow tube and two-ring-fuel-element configuration. The fuel assembly was designed with a two-pass counter-flow configuration, where the coolant travels downward through the central tube and then flows upwards through the fuel elements.

In the case of a no-reheat cycle, there are three potential points of heat extraction that have been studied. The ideal heat extraction location would be the reactor outlet since its temperature is approximately 625 °C. At the other two points, additional sources of heat would be required along with the SCWR process heat.

For a counter-flow double-pipe heat exchanger, the hot and cold fluids will enter the heat exchanger from opposite ends. The hot fluid is the SCW reactor coolant which would flow through the inner pipe. The cold fluid is a separate SCW working fluid flowing through the annulus gap of the heat exchanger. The operating parameters are presented in Table 4. While the 4-stage Cu–Cl cycle only has a maximum temperature requirement of 530 °C, the outlet temperature of the SCW working fluid was set at 600 °C. In the event of a leak in the inner pipe, the SCW working fluid would flow into the inner pipe, thus containing the SCW reactor coolant. Pipe diameters and thicknesses were selected according to ASME standards. As per ASME standards, the design stress of a pressure boundary component is less than a third of the Ultimate Tensile Strength (UTS) of the material. Along with the parameters described in Table 4, the percentage of reactor thermal power to be diverted was set to 10% for a reference case.

Table 4 – Operating parameters for intermediate heat exchanger.

Operating parameter	Inner pipe (hot side)	Annulus gap (cold side)
Fluid	SCW reactor coolant	SCW Working Fluid
Pressure (MPa)	25	25.5
Inlet temperature (°C)	625	350
Outlet temperature (°C)	350	600
Mass flux (kg/m^2 s)	1500	1500
Inner diameter (mm)	20.9	32.5
Outer diameter (mm)	26.7	42.2
Pipe thickness (mm)	2.87	5.80

The reference case used operating pressures of 25 MPa and 25.5 MPa for the hot and cold side, respectively. A mass flux of 1500 kg/(m^2 s) was used for both the hot side and cold side. To achieve the desired heat transfer to the SCW working fluid on the cold side, a total of 256 pipes with a length of 44.6 m per pipe would be needed.

Fig. 11 also demonstrates that at approximately 30 m from the hot side inlet, the temperature profile begins to flatten out. At this point, it is also evident that fluids begin to enter a pseudocritical region. This is shown by the variation in heat transfer coefficient (HTC) profiles after this point. This variation is expected in the pseudocritical region. Fig. 11 also shows rounded peaks in the HTC profile for both the hot side and cold side due to the location of pseudocritical points from the hot side inlet. To remove these variations, the inlet temperature of the cold side and the outlet temperature of the hot side would need to be adjusted. This would keep the operating point of the heat exchanger above the pseudocritical point, thus removing the pseudocritical region.

Depending on the selected production rate, thermal energy requirements of the Cu–Cl cycle may change. As a result, it is important to consider how a different thermal energy requirement will impact the overall size of the heat exchanger. Increasing the amount of energy being diverted from a SCW to a Cu–Cl cycle also increases the size of the heat exchanger.

Cascaded heat pumps for solar thermochemical Cu–Cl cycle

Upgrading heat from nuclear power plants or other industrial waste heat sources up to higher temperatures needed by the Cu–Cl cycle can be achieved through chemical heat pumps [55–57]. Zamfirescu et al. [55] developed a CuCl vapor compression heat pump to meet the highest temperature requirement in the Cu_2OCl_2 decomposition reactor (500–530 °C). The CuCl heat pump requires a bottom heat pump cascaded with it, since its evaporator operates at significantly sub-atmospheric pressure (0.2 mbar) to accommodate source temperatures greater than 480 °C and to achieve an evaporator temperature of 300 °C. Akmahdi [58] developed a cascaded heat pump consisting of a CuCl vapor compression heat pump and a bottom heat pump to upgrade heat from about a 300 °C source temperature to the required temperature of the copper oxychloride decomposition reactor of 500–530 °C.

The cascaded copper (I) chloride – biphenyl heat pump CuCl-$(C_6H_5)_2$ uses a bottom heat pump with biphenyl as a working fluid. Almahdi [58] analysed the temperature, pressure, and mole flow rate of the state points calculated from Aspen Plus. The thermodynamic properties such as molar enthalpy and molar entropy were presented over a range of operating conditions. In Fig. 12, at the lowest pressure of 0.1 bar, the CuCl-biphenyl cascaded heat pump has a lower overall energetic COP (0.52) than the sole biphenyl heat pump (0.85). Its exergetic COP (0.62), however, is greater compared to the exergetic COP (0.52) of the single heat pump. In contrast to the improvement in the CuCl heat pump with the increase of its evaporator pressure, the bottom biphenyl heat pump cycle will experience a reduction in its energetic and exergetic COPs. As the evaporator pressure of the CuCl heat pump increases, high temperature working fluids in the bottom cycle condenser will be expected to evaporate the fluids in the top cycle evaporator. That high temperature source should be provided by the bottom biphenyl heat pump to the CuCl heat pump evaporator which cannot be obtained unless the biphenyl heat sink pressure is raised. This would eventually yield more power consumption and cause COPs to decrease. The CuCl-biphenyl cascaded heat pump will have a similar drop in energetic and exergetic COPs for the same reason.

Solar thermochemical Cu–Cl cycle

In addition to nuclear energy as a potential heat source for the Cu–Cl cycle, another viable source investigated was solar energy [49]. Recent studies [49] examined a solar hydrogen

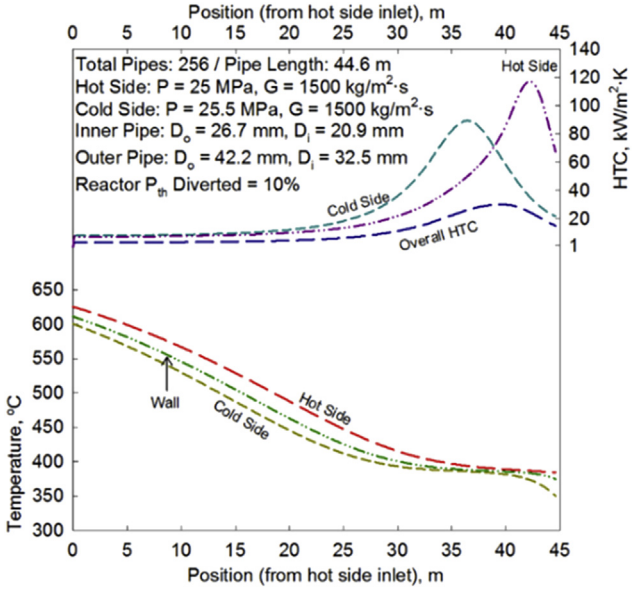

Fig. 11 – Heat transfer coefficient temperature profiles for reference case.

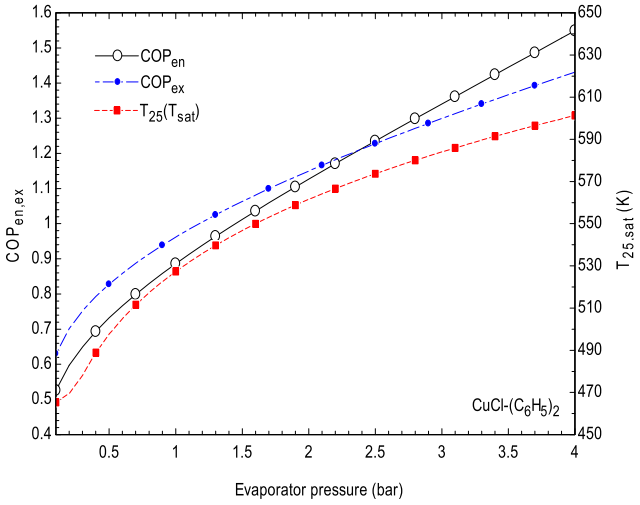

Fig. 12 – Variation of COPs of CuCl-biphenyl cascaded heat pump with biphenyl evaporator pressure.

Table 5 – Design parameters for solar hydrogen plant case study.

Parameters	Value
Solar irradiance (constant, uninterrupted), I	0.8 kW/m^2
Heliostat field diameter, D_{field}	1000 m
Air temperature, T_a	298 K
Air pressure, P_a	0.101 MPa
Wind speed, V_a	1 m/s
Pipe length, L_{pi}	300 m
Turbine inlet temperature, T_{12}	673 K
Turbine inlet pressure, P_{12}	2 MPa
Condenser pressure, P_{13}	0.01 MPa
Cooling water temperature, T_{15}	293 K
Total available solar energy input rate, IA_{field}	785 MW
Total energy rate absorbed by molten salt, $\dot{Q}_{ab}$	309 MW
Estimated hydrogen production rate, $\dot{m}_{H_2}$	0.89 kg/s
Central receiver efficiency, η_{re}	0.49
Thermal efficiency of Rankine cycle, η_{th}	0.26
Production efficiency (H_2 HHV), η_{pr}	0.20

plant consisting of a central receiver, molten salt transport, endothermic Cu–Cl reactions and a Rankine cycle. The central receiver is a parabolic concentrated solar collector that uses a field of heliostat mirrors to focus a large area of energy onto a smaller receiver surface area, resulting in a concentrated radiation input. There are two forms of solar radiation input – beam radiation (or direct normal irradiation) and diffuse radiation. Beam radiation was used for the central receiver of the concentrated solar energy system.

There are two types of losses from the central receiver system: heliostat field losses and receiver losses. The heliostat field losses consist of shadowing, blocking, reflectance and atmospheric attenuation which are related to optical radiation losses. The receiver losses consist of optical radiation losses such as spillage and absorptance as well as thermal losses such as conduction, convection and radiation losses. Table 5 summarizes the parameters used and calculated for a case study of a solar based Cu–Cl plant. The estimated hydrogen production rate and production efficiency for the solar Cu–Cl plant are 0.89 kg H_2/s and 20%, respectively. The total energy input to the solar plant is 785 MW but only 309 MW is absorbed by the molten salt resulting in a central receiver efficiency of 49%. The Rankine cycle efficiency associated with the electrical energy input for the hydrogen production step is about 26%. To simulate the hydrogen plant output accurately, the monthly variations in solar energy input were taken into account. Irradiation values were converted to irradiance by dividing by the daily average hours of daylight for each month taken from the Canadian Weather and Energy Engineering Data Set (CWEEDS).

Conclusions

This paper presented an overview of recent advances in the development and scale-up of the thermochemical Cu–Cl cycle of hydrogen production. It extends previous reports [2–5,16,25] by a Canadian-led international team, including a number of institutions from Canada, U.S., China, Slovenia and Romania. Recent progress was presented for electrochemical cell analysis, membrane characterization, constituent solubility and metastability in ternary mixtures, crystallization measurements, materials corrosion, surface coating performance, system integration, scale-up of unit operations, cascaded heat pumps for heat upgrading, and linkage with solar and nuclear plants. The team's next future goal is an intermediate step of system integration of lab-scale unit operations, followed by a medium term goal of scale-up of the integrated Cu–Cl cycle to a small pilot plant. Ultimately the long term goal is a commercial hydrogen plant in connection with a Generation IV reactor, SCWR (Super-Critical Water Reactor), as part of the Generation IV International Forum (GIF) for hydrogen production with the next generation of nuclear reactors.

Acknowledgements

Support of this research from Canadian Nuclear Laboratories, Ontario Research Excellence Fund and the Natural Sciences and Engineering Research Council of Canada are gratefully acknowledged.

REFERENCES

[1] Lewis MA, Serban M, Basco JK. Hydrogen production at <550°C using a low temperature thermochemical cycle. New Orleans: ANS/ENS Exposition; Nov. 2003.
[2] Naterer GF, Suppiah S, Stolberg L, Lewis M, Wang Z, Rosen MA, et al. Progress in thermochemical hydrogen production with the copper-chlorine cycle. Int J Hydrogen Energy May, 2015;40(19):6283–95.
[3] Naterer GF, Suppiah S, Stolberg L, Lewis M, Ferrandon M, Wang W, et al. Clean hydrogen production with the Cu-Cl cycle – progress of international consortium, I: experimental unit operations. Int J Hydrogen Energy 2011;36:15472–85.
[4] Naterer GF, Suppiah S, Stolberg L, Lewis M, Ferrandon M, Wang W, et al. Clean hydrogen production with the Cu-Cl cycle – progress of international consortium, II: simulations, thermochemical data and materials. Int J Hydrogen Energy 2011;36:15486–501.
[5] Rosen MA, Naterer GF, Chukwu CC, Sadhankar R, Suppiah S. Nuclear-based hydrogen production with a thermochemical copper-chlorine cycle and supercritical water reactor: equipment scale-up and process simulation. Int J Energy Res 2012;36(4):456–65.
[6] Lewis M, Taylor A. High temperature thermochemical processes. DOE hydrogen program, annual progress report, Washington DC. 2006. p. 182–5.
[7] Kasahara S, Kubo S, Hino R, Onuki K, Nomura M, Nakao S. Flow sheet study of the thermochemical tater-splitting iodine–sulfur process for effective hydrogen production. Int J Hydrogen Energy 2007;32(4):489–96.
[8] Carty RH, Mazumder M, Schreider JD, Panborn JB. GRI Report 80-0023. Thermochemical hydrogen production, vol. 1. Chicago, IL: Gas Research Institute for the Institute of Gas Technology; 1981. p. 60616.
[9] Knoche KF, Schuster P, Ritterbex T. Thermochemical production of hydrogen by a vanadium/chlorine cycle. II: experimental investigation of the individual reactions. Int J Hydrogen Energy 1984;9:473–82.
[10] Funk JE. Thermochemical hydrogen production: past and present. Int J Hydrogen Energy 2001;26(3):185–90.

[11] Naterer GF, Dincer I, Zamfirescu C. Hydrogen production from nuclear energy. New York, NY: Springer; 2013. p. 492.
[12] Stolberg L. Electrolysis cell for the conversion of cuprous chloride in hydrochloric acid to cupric chloride and hydrogen gas. US Patent No 0051469. 2010.
[13] Kettner A, Stolberg L, Li H, Shkarupin A, Suppiah S. Electrolysis cell with multiple membranes for CuCl/HCl electrolysis in hydrogen production. Patent Pending, PCT/CA2013/000294. 2013.
[14] Balashov VN, Schatz RS, Chalkova E, Akinfiev NN, Fedkin MV, Lvov S. CuCl electrolysis for hydrogen production in the Cu–Cl thermochemical cycle. J Electrochem Soc 2011;158(3):B266–75.
[15] Ranganathan S, Easton EB. High performance ceramic carbon electrode-based anodes for use in the Cu–Cl thermochemical cycle for hydrogen production. Int J Hydrogen Energy 2010;35(3):1001–7.
[16] Naterer GF, Suppiah S, Stolberg L, Lewis M, Wang Z, Dincer I, et al. Progress of international hydrogen production network for the thermochemical Cu-Cl cycle. Int J Hydrogen Energy January 2013;38:740–59.
[17] Lewis MA, Ahmed S, Lvov S, Fan C. Membrane/electrolyzer development in the Cu–Cl thermochemical cycle. FY 2012 annual report, DOE hydrogen and fuel cells program. 2012.
[18] Edge PSR, Easton EB. Comparison of novel anode materials for the production of hydrogen using CuCl/HCl electrolyzers. ECS Trans 2013;53(9):11–20.
[19] Wang Z, Daggupati VN, Marin G, Pope K, Xiong Y, Secnik E, et al. Towards integration of hydrolysis, decomposition and electrolysis processes of the Cu-Cl thermochemical water splitting cycle. Int J Hydrogen Energy 2012;37:16557–69.
[20] Leray JL. Growth kinetics of hydrated cupric chloride. J Cryst Growth 1968;3:344–9.
[21] Abdel Basir SM. Recovery of cupric chloride from spent copper etchant solution: a mechanistic study. Hydrometallurgy 2003;69:135–43.
[22] Cakir O. Copper etching with cupric chloride and regeneration of waste etchant. J Mater Process Technol 2006;175:63–8.
[23] Yang Z, Huang C, Ji X, Wang Y. New electrolytic method for on-site regeneration of acidic copper (II) chloride etchant in printed circuit board production. Int J Electrochem Soc 2013;8:6258–68.
[24] Ghandehariun S, Rosen MA, Naterer GF, Wang Z. Pinch analysis for recycling thermal energy in the Cu–Cl cycle. Int J Hydrogen Energy 2012;37:16535–41.
[25] Naterer GF, Suppiah S, Stolberg L, Lewis M, Ahmed S, Wang Z, et al. Progress of international program on hydrogen production with the copper-chlorine cycle. Int J Hydrogen Energy 2014;39:2431–45.
[26] O'Connor JJ, Thomasian A, Armington AF. Analysis and solubility of cuprous chloride in hydrochloric acid solutions. J Electrochem Soc Electrochem Sci Sept. 1968:931–2.
[27] Fritz J. Solubility of cuprous chloride in various soluble aqueous chlorides. J Chem Eng Data 1982;27:188–93.
[28] Ferrandon MS, Lewis MA, Tatterson DF, Gross A, Doizi D, Croize L, et al. Hydrogen production by the Cu–Cl thermochemical cycle: investigation of the key step of hydrolysing $CuCl_2$ to Cu_2OCl_2 and HCl using a spray reactor. Int J Hydrogen Energy 2010;35(3):992–1000.
[29] Naterer GF, Suppiah S, Lewis MA, Gabriel KS, Dincer I, Rosen MA, et al. Recent canadian advances in nuclear-based hydrogen production and the thermochemical Cu–Cl cycle. Int J Hydrogen Energy 2009;34(7):2901–17.
[30] Pope K, Naterer GF, Wang ZL. Nitrogen carrier gas flow for reduced steam requirements of water splitting in a packed bed hydrolysis reactor. Exp Therm Fluid Sci 2013;44:815–24.
[31] Daggupati V, Naterer GF, Gabriel K, Gravelsins R, Wang Z. Equilibrium conversion in Cu-Cl cycle multiphase processes of hydrogen production. Thermochim Acta December 2009;496:117–23.
[32] Zamfirescu C, Dincer I, Naterer GF. Thermophysical properties of copper compounds in copper-chlorine thermochemical water splitting cycles. Int J Hydrogen Energy May 2010;35:4839–52.
[33] Xie J, Wang X, Li A, Li F, Zhou Y. Corrosion behaviour of selected Mn+1AXn phases in hot concentrated HCl solution: effect on an element and MX layer. Corros Sci 2012;60:129–35.
[34] Wu D, Mao F, Wang S, Zhou Z. Low-temperature fabrication route for enhancing mechanical properties and corrosion resistance of porous mullite ceramics through homogeneously mullite sol-coating method. Ceram Process 2013;14:677–81.
[35] Sure J, Shankar A, Ramya S, Mudali U. Molten salt corrosion of high density graphite and partially stabilized zirconia coated high density graphite in molten LiCl-KCl salt. Ceram Int 2012;38:2803–12.
[36] Kamali AR, Fray DJ. Molten salt corrosion of graphite as a possible way to make carbon nanostructures. Carbon 2013;56:121–31.
[37] Vignarooban K, Pugazhendi P, Tucker C, Gervasio D, Kannan A. Corrosion resistance of hastelloys in molten metal-chloride heat-transfer fluids for concentrating solar power applications. Sol Energy 2014;103:62–9.
[38] Sellers R, Cheng W, Anderson M, Sridharan K, Wang C, Allen T. Materials corrosion in molten LiF-NaF-KF eutectic salt under different reduction-oxidation conditions. In: Proceedings of ICAPP. Paper 12189; 2012. Chicago: USA.
[39] Siantar E. Study of the effect of molten CuCl immersion test on alloys with high Ni-Content with and without surface coatings. Department of automotive, mechanical and manufacturing engineering, Master's Thesis. Canada: UOIT; 2012.
[40] Orhan MF, Dincer I, Rosen MA. Exergoeconomic analysis of a thermochemical copper-chlorine cycle for hydrogen production using specific exergy cost (SPECO) method. Thermochim Acta 2010;497:60–6.
[41] Orhan MF, Dincer I, Rosen MA. An exergy-cost-energy-mass analysis of a hybrid copper-chlorine thermochemical cycle for hydrogen production. Int J Hydrogen Energy 2010;35:4831–8.
[42] Ozbilen A, Dincer I, Rosen MA. A comparative life cycle analysis of hydrogen production via thermochemical water splitting using a Cu–Cl cycle. Int J Hydrogen Energy 2011;36:11321–7.
[43] Ozbilen A, Dincer I, Rosen MA. Environmental evaluation of hydrogen production via thermochemical water splitting using the Cu-Cl cycle: a parametric study. Int J Hydrogen Energy 2011;36:9514–28.
[44] Haseli Y, Naterer GF, Dincer I. Comparative assessment of greenhouse gas mitigation of hydrogen passenger trains. Int J Hydrogen Energy April 2008;33:1788–96.
[45] Balta MT, Dincer I, Hepbasli A. Exergoeconomic analysis of a hybrid copper-chlorine cycle driven by geothermal energy for hydrogen production. Int J Hydrogen Energy 2011;36:11300–8.
[46] Ratlamwala TAH, Dincer I. Performance assessment of solar based integrated Cu-Cl systems for hydrogen production. Sol Energy 2013;95:345–56.
[47] Wang Z, Naterer GF, Gabriel KS, Secnik E, Gravelsins R, Daggupati V. Thermal design of a solar hydrogen plant with a copper-chlorine cycle and molten salt energy storage. Int J Hydrogen Energy 2011;36:11258–72.

[48] Orhan M, Dincer I, Naterer GF, Rosen MA. Coupling of copper-chlorine hybrid thermochemical water splitting cycle with a desalination plant for hydrogen production from nuclear energy. Int J Hydrogen Energy February 2010;35:1560–74.
[49] Suppiah S, Naterer GF, Rosen MA, Wang Z, Gabriel K, Dincer I, et al. Clean hydrogen production with water splitting technologies. Oshawa, Ontario: ORF Workshop; May 7, 2015.
[50] Abdo Naser, Bradley Easton E. Nafion/Polyaniline composite membranes for hydrogen production in the Cu–Cl thermochemical cycle. Int J Hydrogen Energy 25 May 2016;41(19):7892–903.
[51] Kale SS, Tamhankar SS, Chaudhari RV. Solubility of cuprous chloride in aqueous hydrochloric acid solutions. J Chem Eng Data 1979;24:110–1.
[52] Suppiah S, Naterer GF, Rosen MA, Wang Z, Gabriel K, Dincer I, et al. Clean hydrogen production with water splitting technologies. Oshawa, Ontario: ORF Workshop; June 20, 2016.
[53] Azarbayjani K, Rizvi G, Foroutan F. System development for evaluating performance of corrosion resistant coatings exposed to molten copper chloride salt. Int J Hydrogen Energy 2016;41(19):8386–93.
[54] Azarbayjani K, Rizvi G, Foroutan F. Evaluating effects of immersion tests in molten copper chloride salts on corrosion resistant coatings. Int J Hydrogen Energy 2016;41(19):8394–400.
[55] Zamfirescu C, Naterer GF, Dincer I. Vapor compression CuCl heat pump integrated with a thermochemical water splitting plant. Thermochim Acta 2011;512:40–8.
[56] Zamfirescu C, Naterer GF, Dincer I. Upgrading of waste heat for combined power and hydrogen production with nuclear reactors. ASME J Eng Gas Turbines Power 2010;132(10):102911–9.
[57] Zamfirescu C, Dincer I, Naterer GF. Performance evaluation of organic and titanium based working fluids for high temperature heat pumps. Thermochim Acta 2009;496:18–25.
[58] Almahdi M. Integrated heat pump options for heat upgrading in Cu-Cl cycle for hydrogen production. MASc Thesis, department of mechanical engineering. Oshawa, Ontario: UOIT; 2016.